2D Materials

PAPER • OPEN ACCESS

Carrier transport in two-dimensional topological insulator nanoribbons in the presence of vacancy defects

To cite this article: Sabyasachi Tiwari *et al* 2019 *2D Mater.* **6** 025011

View the article online for updates and enhancements.

IOP ebooks™

Bringing you innovative digital publishing with leading voices to create your essential collection of books in STEM research.

Start exploring the collection - download the first chapter of every title for free.

This content was downloaded from IP address 146.175.11.111 on 08/03/2019 at 10:07

2D Materials

OPEN ACCESS

RECEIVED
8 November 2018

REVISED
10 January 2019

ACCEPTED FOR PUBLICATION
21 January 2019

PUBLISHED
5 February 2019

Original content from this work may be used under the terms of the Creative Commons Attribution 3.0 licence.

Any further distribution of this work must maintain attribution to the author(s) and the title of the work, journal citation and DOI.

PAPER

Carrier transport in two-dimensional topological insulator nanoribbons in the presence of vacancy defects

Sabyasachi Tiwari[1], Maarten L Van de Put[1], Bart Sorée[2,3,4] and William G Vandenberghe[1]

[1] Department of Materials Science and Engineering, The University of Texas at Dallas, 800 W Campbell Rd., Richardson, TX 75080, United States of America
[2] Imec, Kapeldreef 75, 3001 Heverlee, Belgium
[3] Department of Electrical Engineering, KU Leuven, Kasteelpark Arenberg 10, 3001 Leuven, Belgium
[4] Department of Physics, Universiteit Antwerpen, Groenenborgerlaan 161, 2020 Antwerp, Belgium

E-mail: william.vandenberghe@utdallas.edu

Keywords: topological insulators, transistor, quantum transport, defects

Abstract

Using the non-equilibrium Green's function formalism, we study carrier transport through imperfect two-dimensional (2D) topological insulator (TI) ribbons. In particular, we investigate the effect of vacancy defects on the carrier transport in 2D TI ribbons with hexagonal lattice structure. To account for the random distribution of the vacancy defects, we present a statistical study of varying defect densities by stochastically sampling different defect configurations. We demonstrate that the topological edge states of TI ribbons are fairly robust against a high concentration (up to 2%) of defects. At very high defect densities, we observe an increased inter-edge interaction, mediated by the localisation of the edge states within the bulk region. This effect causes significant back-scattering of the, otherwise protected, edge-states at very high defect concentrations (>2%), resulting in a loss of conduction through the TI ribbon. We discuss how this coherent vacancy scattering can be used to our advantage for the development of TI-based transistors. We find that there is an optimal concentration of vacancies yielding an ON–OFF current ratio of up to two orders of magnitude. Finally, we investigate the importance of spin–orbit coupling on the robustness of the edge states in the TI ribbon and show that increased spin–orbit coupling could further increase the ON–OFF ratio.

1. Introduction

Continued scaling has deteriorated the mobility of electronic devices based on three-dimensional (3D) materials [1, 2], resulting in an increasing interest in two-dimensional (2D) materials [3, 4]. The intrinsic 2D structure of these materials offers a great avenue for optimum electrostatic control with sufficient mobility for carrier transport in scaled electronic devices [1]. 2D materials research started with graphene [5], and subsequently expanded to Group IV-based 2D materials [6, 7], transition-metal-dichalcogenides (TMDs) [8], as well as Group V material-based 2D materials like phosphorene [6, 9]. The use of 2D materials in conventional field-effect transistors (FETs) [10, 11], or novel FETs like tunnel-FETs [12, 13] has been explored extensively. Unfortunately success has been limited because 2D material based devices suffer significantly from major growth and process-based limitations, e.g. lattice imperfections and defects [14], mostly vacancy defects [15].

One avenue of research focuses on improving material growth and device fabrication techniques. An alternative avenue, which we will pursue in this paper, is to develop materials and device systems where carrier transport is robust against imperfections. Specifically, we want to exploit topological protection, i.e. robustness against small perturbations, of certain materials properties, while maintaining excellent 2D material electrostatic control. Materials that offer such prospects are 2D topological insulators (TIs) [16].

The 2D TIs we consider are Z_2 TIs that have time-reversal symmetry [17]. Z_2 TIs have an energy band gap in their bulk form, however, in their ribbon form, the energy gap closes and they develop edge states with linear dispersion within an energy window equalling the bulk band-gap. As a result of the time-reversal symmetry, 2D TI ribbons with Z_2 topological order have two counter propagating edge states with their spin

© 2019 IOP Publishing Ltd

and momentum locked. As a consequence, spin-conserving perturbations, i.e. vacancy defects, phonons etc, cannot backscatter the edge states.

2D TIs have been explored extensively in the past decade [18, 19] not only because of their intriguing intrinsic properties, but also because of their possible application in a range of domains such as, charge-based devices, like TI-FETs [16], spin-based devices for, among others, memory applications, [20], and quantum computing applications [21]. Additionally, TIs have also been explored for their application in optoelectronic devices [22, 23].

The TI-FET operates on the principle of the modulation of scattering. In the ON-state of the TI-FET, the Fermi level lies in the centre of the bulk bandgap, resulting in high transmission. In the OFF-state, the Fermi level lies in the bulk state, strongly suppressing transmission. As the bulk state transmission is reduced due to scattering on impurities or due to interaction with other perturbations, the OFF-current of the device is reduced. Therefore, a TI ribbon with a high concentration of vacancy defects can, in principle, lead to a better ON–OFF ratio for TI-FETs. A major advantage of a charge-based device like the TI-FET is its integrability with present-day technology.

2D TIs are ideal for a device like the TIFET because the Fermi level of the TI is modulated using a gate. 3D TIs are 3D materials and have topologically protected surface states instead of edge states like 2D TIs. Gating of 3D TIs is thus very hard since the surfaces are effectively metallic, screening any external electrical field. In 2D materials, gating is comparatively easy and even the edge states can be gated quite effectively due to their low density of states.

At extremely high defect concentrations, however, back-scattering in 2D TIs will occur not only in the bulk but also in the edge states due to inter-edge interactions. Thanks to the localisation of edge states, inter-edge interactions from a small number of non-magnetic defects will be negligible, yielding high transmission through the ribbon. However, in the limiting case of an exceedingly large number of defects, the ribbon will be sundered, resulting in full back-scattering.

In this paper, we theoretically study the effect of point vacancy defects on the carrier transport for a TI ribbon with hexagonal lattice structure and zigzag edge orientation. We quantify the transport of the TI ribbons by calculating the transmission using the non-equilibrium Green's function formalism, presented in section 2. In section 3, we first analyse the effect of the position of a single defect on the transmission of the edge states and bulk states in a TI ribbon. Then, we analyse the effect of the presence of a random distribution of defects, with varying concentration, on the carrier transport in a TI ribbon. We show that the TI edge states are robust for a high defect density (2%). We further show that in the presence of an applied bias, edge states localise around the defect centres within the bulk of the TI ribbon. We demonstrate that a significant amount of inter-edge interaction occurs at defect densities exceeding 4%. Further, we demonstrate that an optimum concentration of vacancy defects gives rise to an ON–OFF current TI-FET ratio of almost 2 orders of magnitude. Finally, we investigate the importance of spin–orbit coupling and a larger energy band gap in ensuring the robustness of the TI edge states. In section 4, we conclude.

2. Methodology

2.1. Electronic Structure of TIs

We model the electronic structure of the 2D Z_2 TI using the tight-binding Kane–Mele Hamiltonian [17] for a hexagonal lattice:

$$H = -t \sum_{\langle i,j\rangle,\alpha} c^\dagger_{i,\alpha} c_{j,\alpha} + \mathrm{i}\Lambda_{\mathrm{so}} \sum_{\langle\langle i,j\rangle\rangle,\alpha,\beta} \nu_{i,j} c^\dagger_{i,\alpha} \sigma^z_{\alpha,\beta} c_{j,\beta} + \mathrm{i}\Lambda_{\mathrm{R}} \sum_{\langle i,j\rangle,\alpha,\beta} c^\dagger_{i,\alpha} (\sigma \times \hat{d}_{i,j})^z_{\alpha,\beta} c_{j,\beta}, \quad (1)$$

where the first term, with coupling strength t, accounts for the nearest neighbour hopping, $\langle i,j\rangle$, between adjacent lattice sites i and j, with respective electron creation and annihilation operators $c^\dagger_{i,\alpha}$, $c_{j,\alpha}$. α and β represent spin degrees of freedom, i.e. $\alpha \in \{\uparrow,\downarrow\}$ and $\beta \in \{\uparrow,\downarrow\}$. The second term, with coupling strength given by the spin–orbit coupling magnitude Λ_{so}, accounts for the next nearest neighbour hopping $\langle\langle i,j\rangle\rangle$ with Pauli matrix σ_z. The parameter $\nu_{i,j}$ is $+1$ when the shortest nearest neighbor path from i to j is clockwise, and -1 if it is counterclockwise. The third, and final, term, with coupling strength Λ_{R}, accounts for the Rashba spin–orbit interaction, which accounts for the out-of-plane symmetry breaking of the 2D TI lattice, which can be induced by a perpendicular electric field or the interaction with an underlying substrate.

Since we do not consider such out-of-plane symmetry breaking effects in the current work, we can safely ignore the Rashba spin–orbit interaction, i.e. $\Lambda_{\mathrm{R}} = 0$. This Kane–Mele Hamiltonian preserves time-reversal symmetry and can model both a trivial ($\Lambda_{\mathrm{so}} = 0$) or a non-trivial Z_2 ($\Lambda_{\mathrm{so}} > 0$) band ordering.

To obtain realistic parameters for the Kane–Mele Hamiltonian, we fit the various coupling parameters to model stanene, a hexagonal monolayer of tin, which is a 2D topological insulator with a theoretically predicted band-gap of 0.1 eV [24, 25]. To obtain a reference bandstructure, we use density functional theory (DFT), as implemented in the Vienna *ab initio* simulation package (VASP) [26, 27]. The DFT bandstructure is obtained using a projector-augmented wave (PAW) potential [27] with a generalised-gradient approximation (GGA) exchange-correlation as proposed by Perdew–Burke–Ernzerhof (PBE) [28]. A $11 \times 11 \times 1$ **k**-grid sampling is used and the energy cut-off is set to 240 eV.

By fitting the stanene bulk bandstructure obtained using DFT with the tight-binding bandstructure

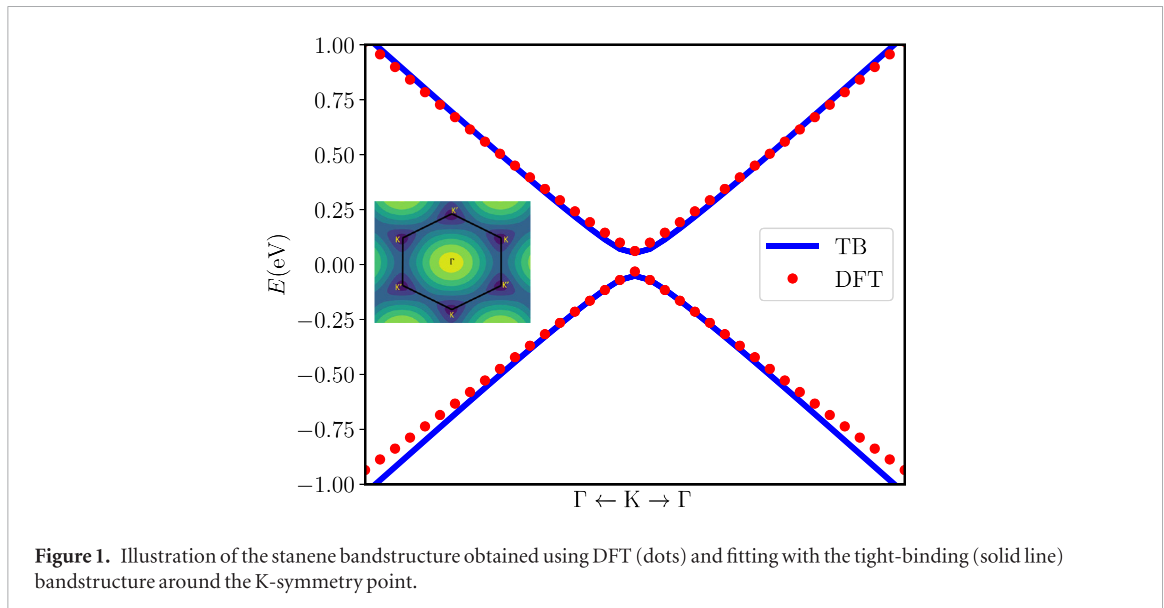

Figure 1. Illustration of the stanene bandstructure obtained using DFT (dots) and fitting with the tight-binding (solid line) bandstructure around the K-symmetry point.

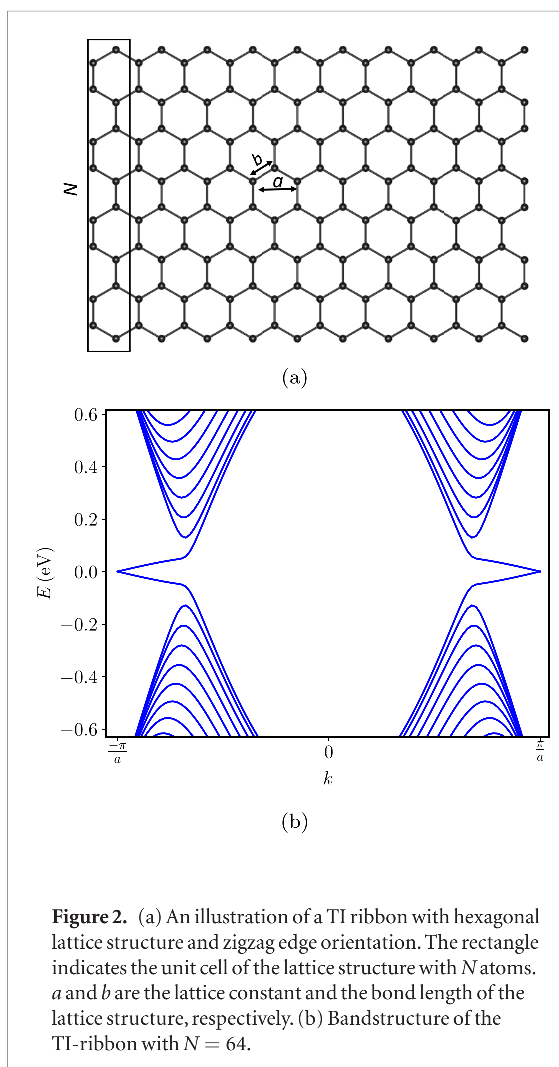

Figure 2. (a) An illustration of a TI ribbon with hexagonal lattice structure and zigzag edge orientation. The rectangle indicates the unit cell of the lattice structure with N atoms. a and b are the lattice constant and the bond length of the lattice structure, respectively. (b) Bandstructure of the TI-ribbon with $N = 64$.

obtained by diagonalizing the Kane–Mele Hamiltonian for a periodic unit cell, we obtain the nearest neighbour coupling parameter $t = 0.85$ eV, as well as the spin–orbit coupling term $\Lambda_{so} = 10$ meV. Figure 1 shows the bulk stanene bandstructure obtained with DFT and the fitted Kane–Mele band structure. Unless explicitly stated, all presented results use the parameters obtained for stanene.

2.2. Ribbons

The Hamiltonian matrix for a TI ribbon is constructed, atom by atom, from the tight-binding Kane–Mele Hamiltonian (1). A pristine TI ribbon with a zigzag edge consists of a repetition of a 'unit cell', containing N atoms each. To construct a ribbon with a given length, the unit cell is repeated N_{cell} times. An illustration of one such ribbon with its unit cell is shown in figure 2(a). As the Kane–Mele Hamiltonian accounts for two spin components at each atom, the square Hamiltonian matrix is of size $2 \times N_{\text{cell}} \times N$. However, since the Hamiltonian only has the nearest neighbour and next-nearest neighbour coupling, the resulting matrix is sparse, containing only 10 nonzero elements per row. The first (left) and last (right) unit cell of the ribbon, containing N atoms, are treated as the left and the right contact of the ribbon and represent an infinite continuation of the ribbon.

Figure 2(b) shows the band structure of the hexagonal-zigzag TI ribbon calculated using the periodic repetition of the unit cell shown in figure 2(a). We see the edge state spectrum with a linear dispersion at the zone boundaries ($k = \pm\pi/a$).

2.3. Modeling vacancy defects

To model a vacancy defect at site R, we change the local Hamiltonian to that of a trivial insulator,

$$H_{\text{v}} = V_{\text{v}} \sum_{R,\alpha} c^{\dagger}_{R,\alpha} c_{R,\alpha} + t_{\text{v}} \sum_{\langle R,i \rangle,\alpha} c^{\dagger}_{R,\alpha} c_{i,\alpha}, \qquad (2)$$

where t_{v} is the coupling strength between the vacancy site and its nearest-neighbour lattice sites i and V_{v} is the on-site potential. The on-site potential (V_{v}) for vacancies has been set to the work-function of stanene (4.5 eV), which we extract from the DFT results of a stanene sheet [29]. We set the vacancy coupling

strength to correspond to the coupling of a free electron in vacuum,

$$t_v = \frac{\hbar^2}{2m_e b^2} \approx 0.51 \text{ eV}, \tag{3}$$

where $\hbar$ is the reduced Planck constant, m_e is the free electron mass and $b = c\cos(\theta)$ is the in-plane projection of stanene's buckled bond, where stanene's bond length is $c = 2.8$ Å and the buckling angle is $\theta = 16.86°$.

2.4. Random defect generation

To generate a given concentration of defects in a TI ribbon, we generate the locations of the defects using a uniform pseudorandom generator, excluding the contact regions, which always represent semi-infinite pristine leads. After removing the atoms at the defect sites, we scan the lattice for atoms that have more than one dangling bond. Since atoms with more than one dangling bond are unphysical and will likely not be structurally stable, we remove such occurrences. Finally, for each removed atom, we change the ribbon Hamiltonian from the topological Kane–Mele form to the vacancy form given in (2).

2.5. Transport model

To study the transport of carriers in the TI ribbon, we use the non-equilibrium Green's function formalism [30]. Within this formalism, we calculate the retarded Green's function, G^r, and the advanced Green's function, G^a, as,

$$G^r(E) = [EI - H - \Sigma_R(E) - \Sigma_L(E)]^{-1}, \tag{4a}$$

$$G^a(E) = [G^r(E)]^\dagger, \tag{4b}$$

where H is the Hamiltonian of the TI ribbon, E is the energy at which the Green's functions are calculated, I is an identity matrix and $\Sigma_L(E)$ and $\Sigma_R(E)$ are the respective left and right contact self-energies that describe the open boundary conditions with infinite leads.

We employ the quantum transmitting boundary method (QTBM) [31] to calculate the contact self-energies. To obtain the self-energy matrices for an atomistic structure, we have to separate out injected modes at the leads based on their direction of motion. Therefore, we have to find the homogeneous solutions in the left (L) and right (R) leads that obey $\phi_{L/R} = \lambda_{L/R}\phi_{L/R}$ by solving the second order eigenvalue problem at an energy E,

$$\left(W_-\lambda_{L/R}{}^2 + H_0\lambda_{L/R} + W_+\right)\phi_{L/R} = E\,\lambda_{L/R}\phi_{L/R} \tag{5}$$

which we obtain by the nearest neighbour expansion of the tight-binding Hamiltonian in the leads. Here, $\phi_{L/R}$ has $2 \times N$ components, two spin orientations at each lattice site. W_-, W_+ are the left and the right hopping matrices for the lead unit cell. The periodicity of the wave-function is taken into account by the phase factor $\lambda_{L/R} = \exp(-ika)$ that sets the wave vector k in the transport direction. H_0 is the onsite matrix block, determined as the first (left) or last (right) $2N \times 2N$ block of the ribbon Hamiltonian. To solve the quadratic eigenvalue problem, we linearize it to a generalized eigenvalue problem of double rank,

$$\begin{bmatrix} 0 & I \\ -W_+ & EI - H_0 \end{bmatrix}\begin{bmatrix} \phi_{L/R} \\ \lambda\phi_{L/R} \end{bmatrix} = \lambda_{L/R}\begin{bmatrix} I & 0 \\ 0 & W_- \end{bmatrix}\begin{bmatrix} \phi_{L/R} \\ \lambda\phi_{L/R} \end{bmatrix}. \tag{6}$$

In the solutions of the above generalised eigenvalue problem, we distinguish three cases, $|\lambda_{L/R}| = 1$, $|\lambda_{L/R}| > 1$ and $|\lambda_{L/R}| < 1$. Solutions where $|\lambda_{L/R}| > 1$, correspond to modes that are divergent in the leads. Solutions where $|\lambda_{L/R}| < 1$, correspond to evanescent modes that are non-divergent in the leads. Solutions where $|\lambda_{L/R}| = 1$ represent travelling modes that are either outgoing (group velocity > 0) or incoming (group velocity < 0). We determine the group velocity of a mode using the Hellmann–Feynman method [32].

In figure 3, we show the band structure of the contacts, obtained by plotting only the running waves of the complex bandstructure, with an indication of outgoing and incoming modes. As the contacts are the infinite repetition of the leads, the obtained bandstructure is identical to the band structure of the TI ribbon, shown in figure 2(b).

The self-energy matrices are constructed from the evanescent and outgoing traveling modes. From the eigenvalues ($\lambda_{L/R}$) and the eigenvectors ($\phi_{L/R}$) of the modes corresponding to decaying and outgoing waves in each lead, the self-energy matrices for an energy E are calculated using,

$$\Sigma_{L/R}(E) = W_-\Phi_{L/R}\Lambda_{L/R}\Phi_{L/R}^{-1}, \tag{7}$$

where $\Phi_{L/R}$ is a matrix whose columns comprise the wave-functions $\phi_{L/R}$. $\Lambda_{L/R}$ is a diagonal matrix comprising of the eigenvalues obtained as $\lambda_{L/R}$.

We calculate the transmission from the left contact to the right within the Green's function formalism using,

$$T(E) = \mathrm{Tr}(\Gamma_L G^r \Gamma_R G^a), \tag{8}$$

where the contact broadening matrices are calculated as $\Gamma_{R/L}(E) = \mathrm{i}[\Sigma_{R/L}(E) - \Sigma_{R/L}^\dagger(E)]$.

The local density of states (LDOS) at a given energy E is determined by the diagonal of the spectral function,

$$A_{L/R}(E) = G^r\Gamma_{L/R}G^a. \tag{9}$$

The energy-resolved local current, which we will call the local spectral current, between lattice sites i and j, and spin $\alpha \in \{\uparrow, \downarrow\}$ is given as,

$$I_{i,j,\alpha}(E) = -\frac{e}{\hbar}\mathrm{Im}(G^<_{i,j,\alpha}H_{i,j,\alpha} - H_{j,i,\alpha}G^<_{j,i,\alpha}), \tag{10}$$

where e is the electron charge and $G^<_{i,j,\alpha}$ is the lesser Green's function,

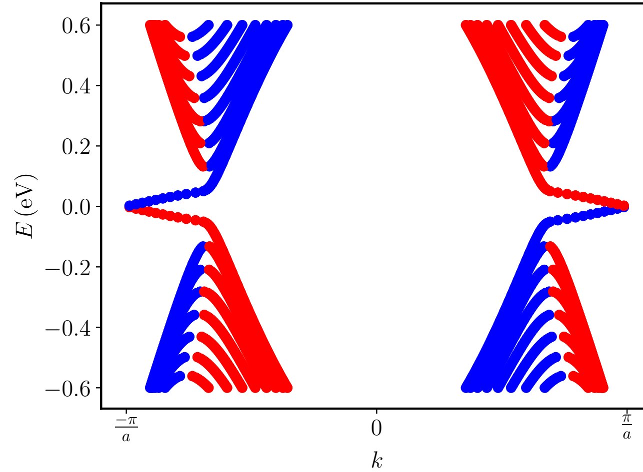

Figure 3. Illustration of the bandstructure obtained for a 12.7 nm wide TI ribbon with hexagonal lattice structure and zigzag edge, obtained from QTBM. a is the lattice constant as shown in figure 2(a). Blue dots show electrons moving with positive velocity and the red dots show electrons moving with negative velocity.

$$G^{<}(E) = A_{\mathrm{L}} f(E - \mu_{\mathrm{L}}) + A_{\mathrm{R}} f(E - \mu_{\mathrm{R}}), \quad (11)$$

where $f(E)$ is the Fermi–Dirac distribution and $\mu_{\mathrm{L/R}}$ is the electrochemical potential of the respective contact. The local spectral current is calculated for a bias, $\Delta V = \mu_{\mathrm{L}} - \mu_{\mathrm{R}}$, applied between the two contacts of the TI ribbon. Note that this bias is only applied to the electrochemical potential and that the electrostatic potential throughout the wire is assumed to be flat.

The calculated spin-resolved local spectral current is projected into Cartesian coordinates by decomposing the current, $I_{i,j,\alpha}(E)$ from one lattice site i to the other lattice site j, into its local Cartesian components,

$$I_{\mathrm{x},\alpha}(E) = I_{i,j,\alpha}(E)\cos(\theta_{i,j}), \quad (12a)$$

$$I_{\mathrm{y},\alpha}(E) = I_{i,j,\alpha}(E)\sin(\theta_{i,j}), \quad (12b)$$

where $\theta_{i,j}$ is the angle between lattice sites i and j. To avoid double counting, the local spectral current is only projected for $I_{i,j,\alpha}(E) > 0$, between lattice sites i and j. This current is then plotted on the mesh corresponding to the atomic position of the atoms in the ribbon. The total local spectral current, which we will call the local spectral charge current, is obtained by summing over the spin degrees of freedom $\alpha \in \{\uparrow, \downarrow\}$,

$$I_{i,j}(E) = I_{i,j,\uparrow}(E) + I_{i,j,\downarrow}(E). \quad (13)$$

3. Results and discussion

3.1. Transport through pristine ribbon

We first simulate the carrier transport in a pristine TI ribbon, as illustrated in figure 4(a). In all simulations reported in this paper, the TI ribbon is 12.83 nm wide 23.7 nm long. The calculated transmission for this ribbon is shown in figure 4(b). For a pristine ribbon, the transmission is simply equal to the number of modes. The edge states, with energies in the bulk bandgap, have a transmission equal to two, one for each edge state or, equivalently, one for each spin-channel. The bulk band gap, obtained from the low energy approximation of the Kane–Mele Hamiltonian, measures $E_{\mathrm{g}} = 2\Delta_{\mathrm{so}} = 6\sqrt{3}\Lambda_{\mathrm{so}}$. With $\Delta_{\mathrm{so}} = 0.05$ eV for stanene, we find the edge states within an energy window of ± 0.05 eV. The energy states outside this energy window are the bulk states.

In figure 5(a), the spectral function for a state with $E \approx 0$ eV[5], i.e. at the Dirac point is shown. The spectral function reveals the edge states localised on both edges of the TI ribbon. The local spectral charge current, depicted in figure 5(b), shows that the flow of the current through the edge states is unidirectional.

Figure 5(c) shows the comparison between the LDOS of the edge states, injected at energies 2 meV and 25 meV. We observe that the edge states injected at an energy closer to the Dirac point are more localised. The localisation of the wavefunctions of the edge state is directly proportional to the spin–orbit coupling strength Λ_{so}, which will be discussed in the subsequent sections. However, the localisation of the edge state wavefunction decreases as the energy approaches the bulk conduction or valence band. This is in line with the previously reported, 'evolution' of the edge state LDOS with increasing energy [33].

3.2. Effect of a single point defect

Next, we investigate the impact of a single defect in the TI ribbon, either in the centre or at the edge, as illustrated in figure 6(a). Figure 6(b) shows a comparison between the transmission of the pristine ribbon with a ribbon with a single defect in the centre (bulk defect) and at the edge (edge defect). We see that the transmission for the edge states, in the −50 meV to 50 meV range remains unaffected, both for the edge defect and the bulk defect case. However, the bulk state transmission is affected by both defects, in particular

[5] For all $E \approx 0$ eV we used $E = 2$ meV in our calculations. Exactly at $E = 0$ eV, a small gap opens due to the finite size of the ribbon.

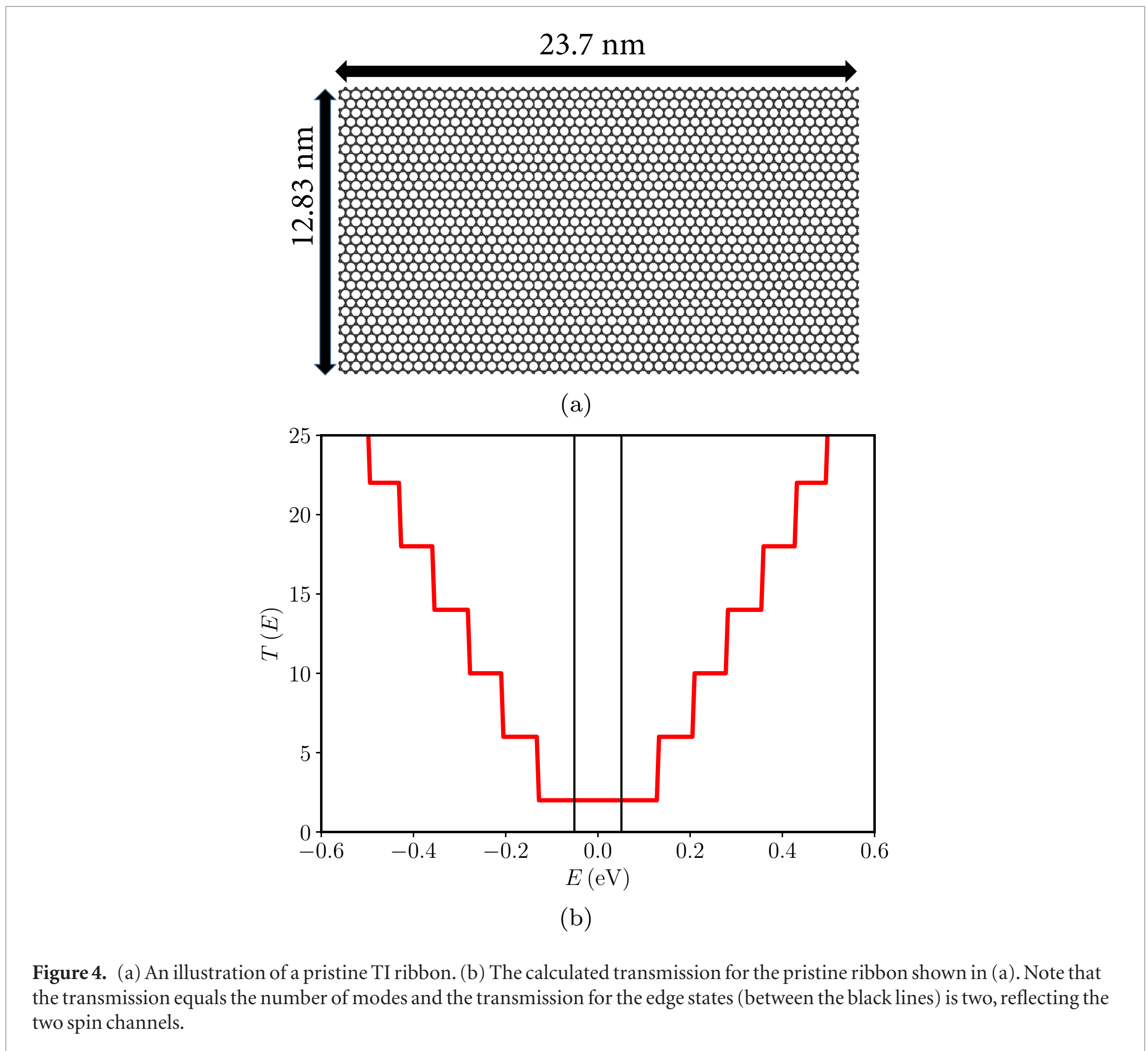

Figure 4. (a) An illustration of a pristine TI ribbon. (b) The calculated transmission for the pristine ribbon shown in (a). Note that the transmission equals the number of modes and the transmission for the edge states (between the black lines) is two, reflecting the two spin channels.

for higher energy states. The bulk state behaviour is in agreement with scattering theory since the states extend across the entire ribbon width, their first-order matrix element with the vacancy Hamiltonian is significant. We also observe an asymmetry in the transmission spectrum around the Dirac cone energy ($E = 0$), both for the edge and the bulk defect. This behaviour is observed because the vacuum potential used at the defect sites is positive, breaking the symmetry of the Kane–Mele Hamiltonian with respect to energy.

Figure 7 shows the up-spin component of the spectral function for the edge-state calculated for the ribbon with an edge defect. The up-spin component is localised on the bottom edge, and we observe that the edge state is not reflected, but flows around the defect instead. This lack of back-scattering is a consequence of spin and momentum locking combined with the vacancy Hamiltonian. Inter-edge scattering on the other hand, requires a significant overlap between the wavefunctions of states of the opposite edge with the vacancy Hamiltonian. However, the edge state wavefunctions decay exponentially in the bulk, with a decay length of the order of one nanometer, ensuring minimal back-scattering in the presence of a single defect.

The interaction with a single defect increases the extent of the edge state wavefunction and facilitates a path for backscattering through multiple defects, as discussed next.

3.3. Effect of the random distribution of vacancy defects

In a realistic material, the lattice has a significant number of defects which we assume to be distributed randomly. We have shown, in the previous section, that a single point defect results in only negligible inter-edge interaction. However, a cumulative effect of multiple point defects, distributed randomly in the lattice structure could lead to a significant amount of inter-edge interaction. Therefore, to fully account for the random nature of the defect locations, we perform a statistical study of representative samples with the same defect concentration.

For our study, we distribute random vacancy defects in the 2D TI ribbon, removing 0.5%, 1%, 2%, 3%, 4%, 5%, 7%, 10% of the total number of atoms. For each concentration, we simulate 50 different, randomly sampled, configurations. Examples of two configurations of a TI ribbon with a defect density of 2% and 4% can be found in figures 9(a) and 10(a). As before, we quantify the transport through these

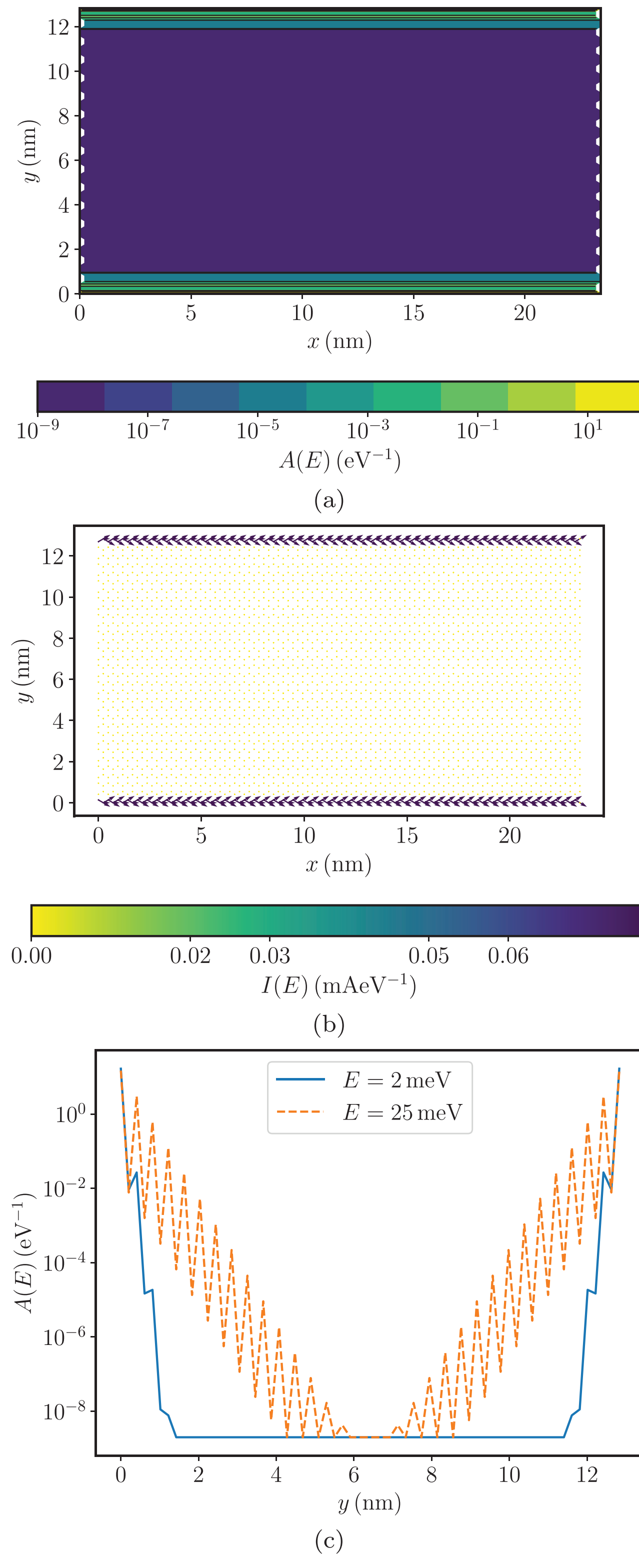

Figure 5. (a) The spectral function for a pristine ribbon calculated for $E \approx 0$ revealing the edge states. (b) The local spectral charge current for current injected from the left side with $E \approx 0$ eV. (c) A comparison of the spectral function, calculated at $E \approx 0$ meV and $E = 25$ meV, accross the width of the ribbon at $x = 10$ nm.

defective TI ribbons by calculating the transmission. In figure 8, we collect the transmission results for each density. The median value of the transmission of the ensemble of configurations is shown as a solid line while the shaded area covers the 25th to the 75th percentile of the obtained transmission coefficients. We show the percentile instead of the standard deviation because the transmission results are not normally distributed and have a well-defined upper and lower limit, i.e. the edge state transmission ranges from zero to two.

Analyzing figure 8 more closely, we see that the transmission of the edge states for energies close to zero, remains almost unchanged compared to the pristine TI ribbons for defect densities up to 1%. However, we

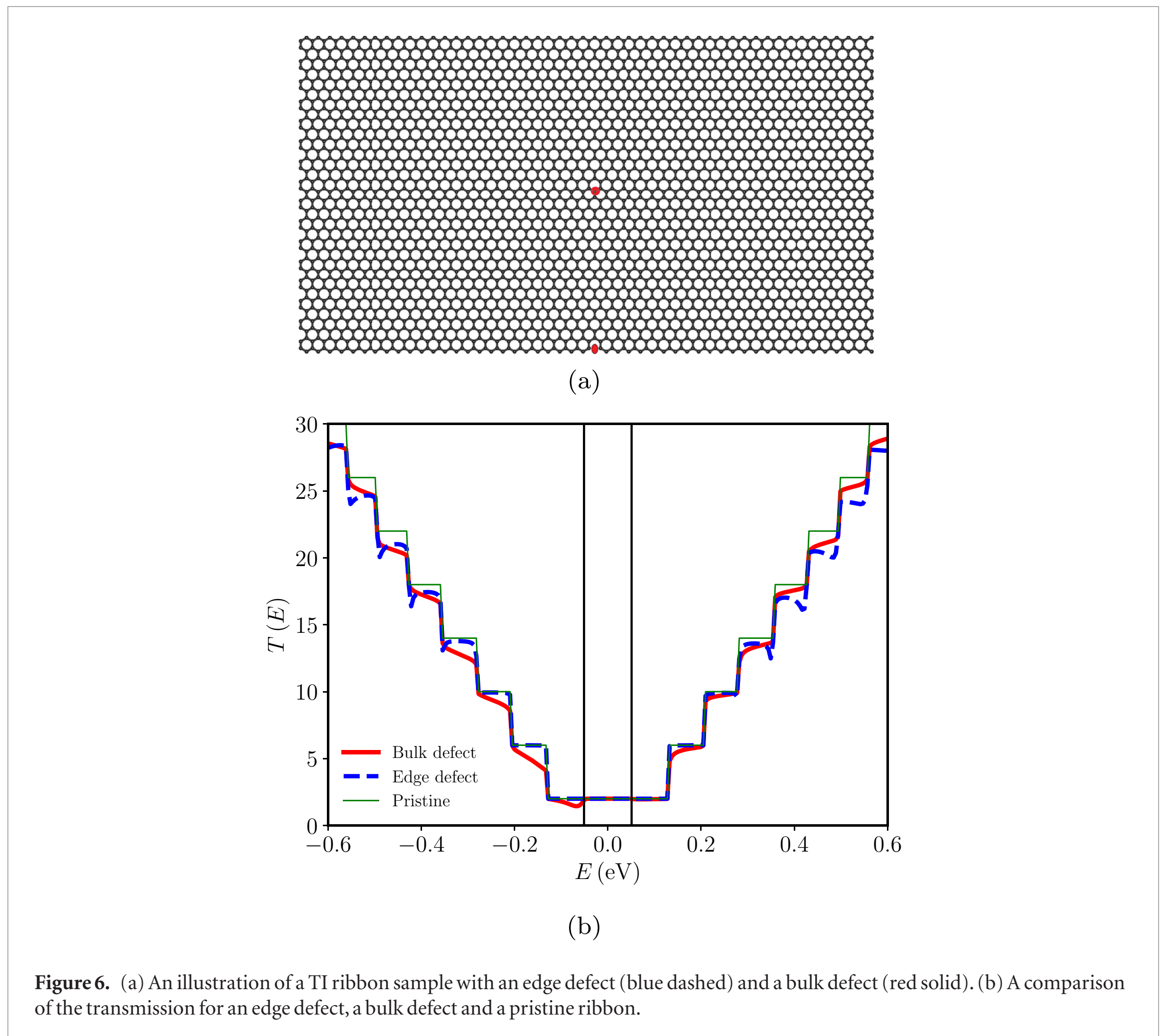

Figure 6. (a) An illustration of a TI ribbon sample with an edge defect (blue dashed) and a bulk defect (red solid). (b) A comparison of the transmission for an edge defect, a bulk defect and a pristine ribbon.

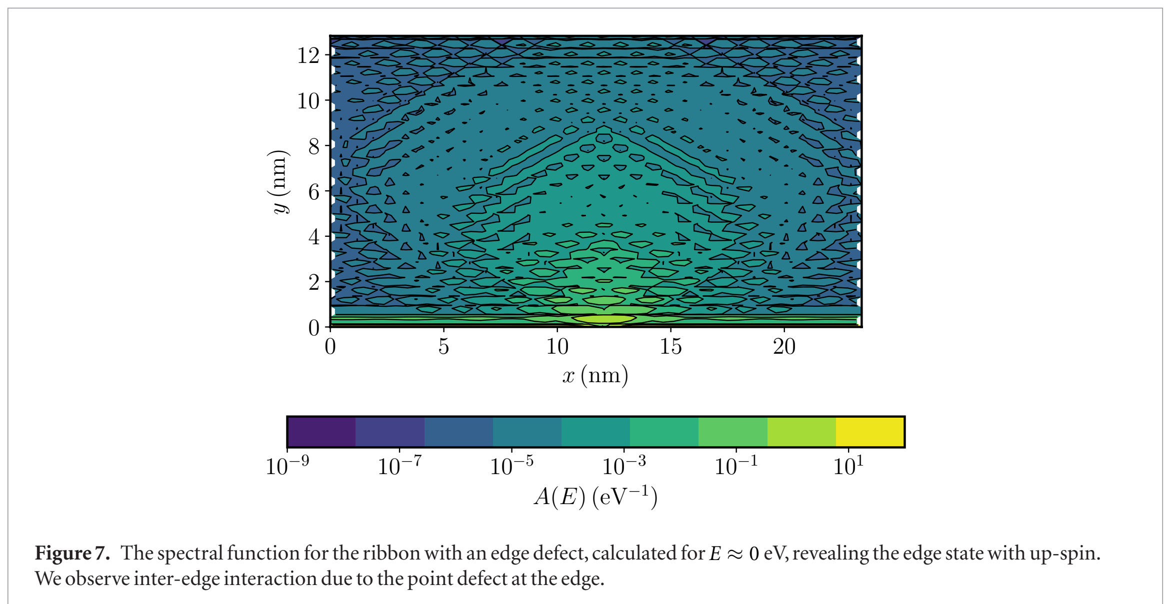

Figure 7. The spectral function for the ribbon with an edge defect, calculated for $E \approx 0$ eV, revealing the edge state with up-spin. We observe inter-edge interaction due to the point defect at the edge.

observe a sharp decrease in the edge state transmission when the defect density reaches 4% and an almost complete transmission suppression at 10%. In the intermediate regime, at around 2% defect density, we see that the edge state transmission remains intact around the Dirac point but quickly decreases for energies away from the Dirac point. This decrease in transmission is related to the inter-edge interaction which is most strongly suppressed at the Dirac point, where the edge state decay length is the shortest. Turning our attention towards the bulk states, we see that their transmission reduces significantly for even small defect densities. This is in line with our findings for a single defect in the previous section. Bulk state transmission suffers due to the backscattering on defect centres along with the localisation around them [34]. However, the same is

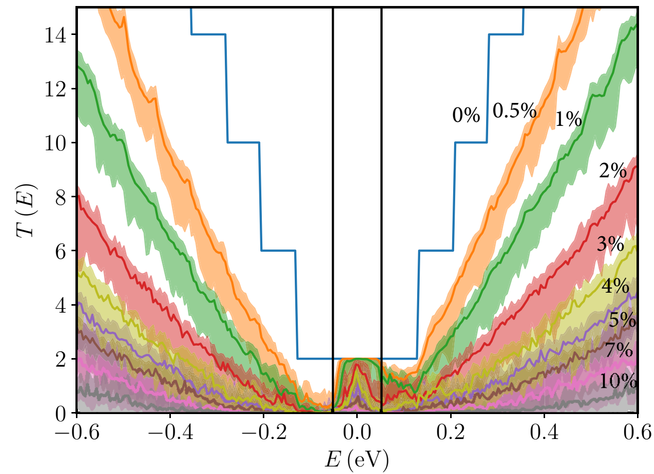

Figure 8. A comparison of the transmission for a defect density of 0% (pristine), 0.5%, 1%, 2%, 3%, 4%, 5%, 7% and 10%. The solid line shows the median and the shaded region shows the 25th to the 75th percentile of the transmission for each defect density.

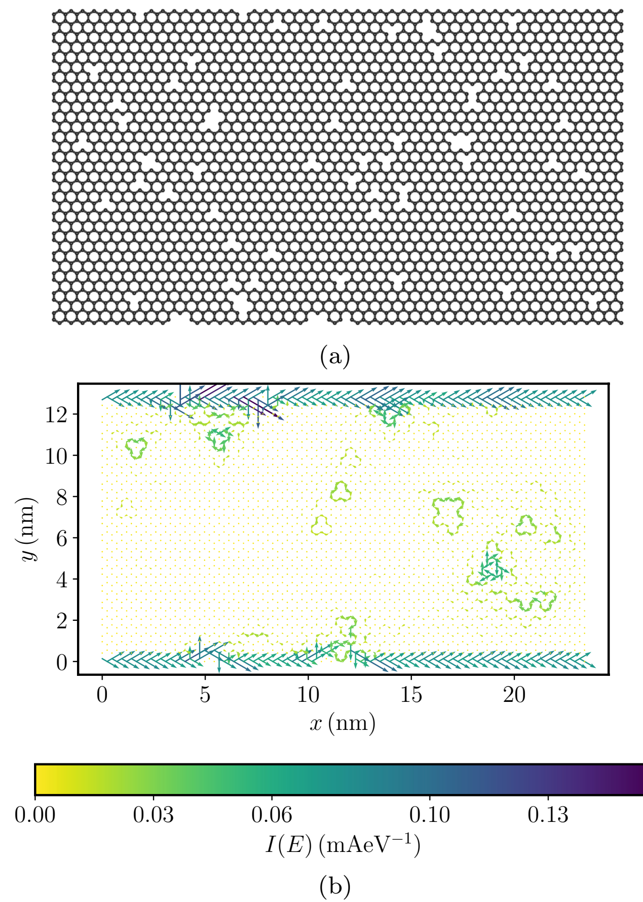

Figure 9. (a) An illustration of a TI ribbon with a defect density of 2%. (b) The local spectral charge current calculated at $E \approx 0$ eV with an injection from the left side.

not the case with the edge states and, hence, a significant drop in the edge state transmission occurs only when the defect density exceeds 4%.

To study the scattering mechanism of the edge states in more detail, we compare a single random defect configuration for a TI ribbon with 2% defect density in figure 9 to a ribbon with a 4% defect density in figure 10.

For the 2% defect density case, the local spectral charge current is shown in figure 9(b). The current is mainly localised at the edges of the ribbon, as in a pristine ribbon, confirming the high transmission. However, figure 9(b) already shows that the edge state interacts with the vacancies, where a small portion of the current appears to be localised in the bulk region of the ribbon, around the vacancies. The defects within the

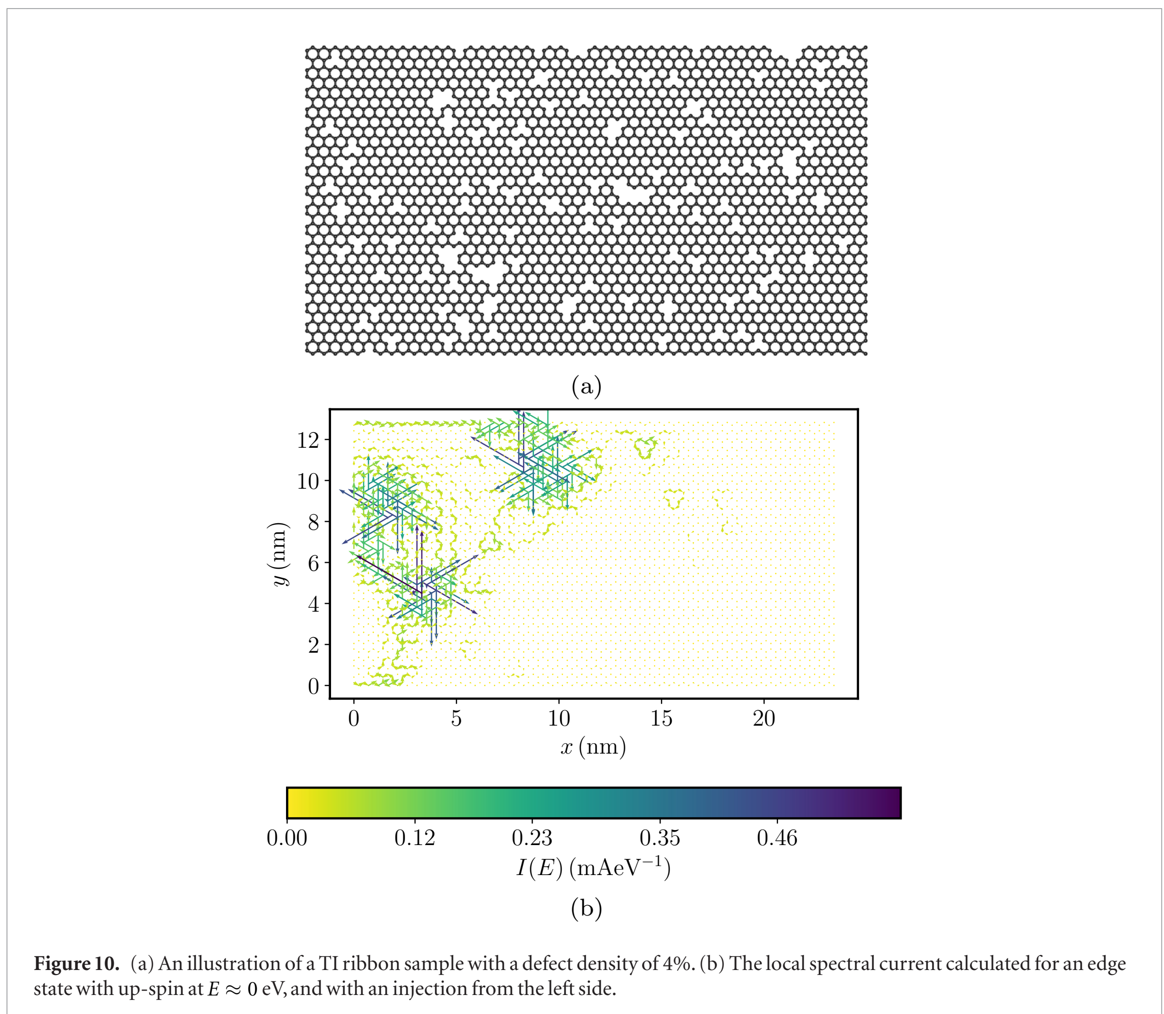

Figure 10. (a) An illustration of a TI ribbon sample with a defect density of 4%. (b) The local spectral current calculated for an edge state with up-spin at $E \approx 0$ eV, and with an injection from the left side.

bulk of the ribbon act as an edge that can also sustain, extremely localised, topological edge states. Since these edge states form around a defect centre, they are localised and form a current loop. When an injected edge state interacts with such a localisation centre, a current vortex, with non-vanishing curl, appears around the defect. The cyclic orientation (clockwise/anticlockwise) depends on the spin polarization (up/down) of the edge state that interacts with it. A similar effect has been found in the context of the BHZ Hamiltonian [35] and for other models of topologically non-trivial insulators in [36, 37].

Next, we turn to the case of 4% defect density, as shown in figure 10. In figure 10(b), we show the local spectral current for the up-spin edge state at the Dirac point. As expected from our discussion of the transmission spectrum, we see a significant amount of backscattering of the injected carriers. The carriers injected at the bottom edge strongly interact with the defects in the bulk region and get scattered to the top edge, where they travel back into the originating contact. It is clear that this back-scattering is mediated by the localised edge states around the defect centres, providing 'stepping stones' for scattering from one edge to the other. The proximity of defect centres to each other thus significantly increases the amount of inter-edge interaction. This augmented inter-edge interaction, in turn, leads to a significant drop in the transmission due to backscattering. We have verified that this effect is prevalent in most TI ribbon samples with greater than 4% defect density. This cumulative effect of inter-edge interaction and bulk localisation explains why, at high defect densities, TI ribbons suffer from a lower transmission compared to lower defect densities, where defects are generally far apart.

Finally, note that in all cases, localised vortices of the edge states can appear around defects. In an equilibrium state, the injection of carriers from both the leads is equal and each edge has equal but counter-propagating spin-polarized carriers. Therefore, no net current flows, nor is there any non-vanishing current curl in the ribbon. Carriers with up-spin and down-spin revolve equally with opposing directions around a defect centre. However, with an applied bias, the injection from the contacts is not symmetric and one edge exhibits a net up-spin while the other edge has a net down-spin. Since defects will couple more strongly with one edge compared to the other, e.g. due to their location or due to the interaction with other defects, a net curl of the current will be present under the application of bias. This non-vanishing curl will generate a small localised magnetic field, in addition to the spin imbalance.

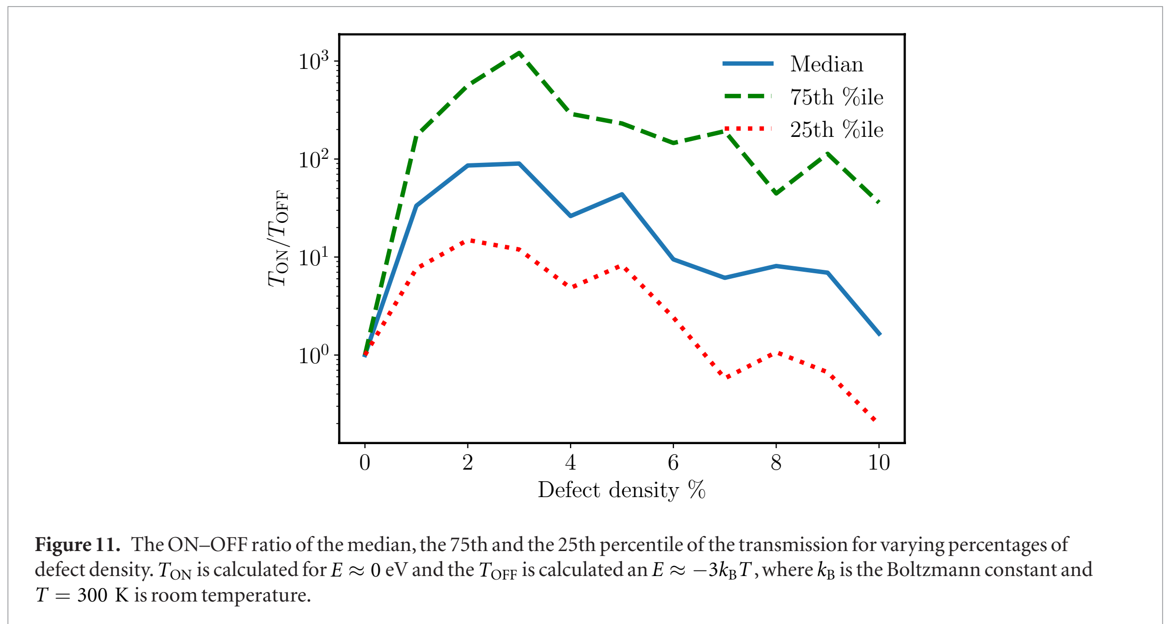

Figure 11. The ON–OFF ratio of the median, the 75th and the 25th percentile of the transmission for varying percentages of defect density. T_{ON} is calculated for $E \approx 0$ eV and the T_{OFF} is calculated an $E \approx -3k_BT$, where k_B is the Boltzmann constant and $T = 300$ K is room temperature.

3.4. An application: the TI-FET

In figure 8, we see a sharp drop of the bulk state transmission around $E \approx \pm 0.05$ eV for defect densities ranging from 0.5% to 5%. As introduced before, Vandenberghe *et al* [16] previously presented a TI-FET concept which uses TI ribbons as the channel material and relies on a reduced transmission of the bulk states. The TI-FET operating principle relies on the modulation of scattering through external gate action. Where in the ON-state of the TI-FET, the Fermi level lies in the centre of the bulk bandgap, resulting in high transmission, in the OFF-state, the Fermi level lies in the bulk state, strongly suppressing transmission. As the bulk state transmission is reduced due to scattering on impurities or due to interaction with other perturbations, such as the electron–phonon interaction, the OFF-current of the device is reduced. The TI-FET's performance will eventually depend on the ratio of transmission through the edge states versus the transmission through the bulk states.

To assess the promise of vacancy defects as (one of) the scattering mechanisms of the TI-FET, we calculate the ratio of the transmission for an edge state (T_{ON}) at the Dirac cone ($E \approx 0$ eV) and a bulk-state (T_{OFF}) at $E \approx -0.075$ eV for defect densities ranging from 0% to 10% for each integer percentage. These energy values have been chosen, such that the switching voltage is around $3k_BT$ at room temperature ($T = 300$ K), where k_B is the Boltzmann constant. As before, we simulate 50 different configurations for each defect density. Figure 11 shows the median, 25th and 75th percentile of the T_{ON}/T_{OFF} ratio plotted against the corresponding defect density. We see that the median of the ratio reaches the maximum value $\approx 10^2$ for a defect density of 3% and reduces to $\approx 10^0$ for a defect density of 10%. As seen in figure 11, our model predicts that a defect density of 3% is optimal for observing a good T_{ON}/T_{OFF} ratio for the selected TI-ribbon configuration (width and parameters). Since TI-FET current is directly proportional to the transmission, we can estimate that for a small bandgap 2D TI such as stanene (with $\Delta so = 0.05$ eV), coherent scattering on vacancies alone can be expected to result in an ON–OFF current (I_{ON}/I_{OFF}) ratio of up to two orders of magnitude for an average device, with an optimized defect density.

From an application perspective, however, a major problem lies in the large variability between T_{ON}/T_{OFF} ratio of the TI-ribbons as it ranges from $\approx 10^1$ to $\approx 10^3$, in the 25th to 75th percentile alone. This variability stems from the strong dependence of the relative position of the defects with respect to the edge and with respect to each other. We have shown that a random configuration of defects can cause localisation of the edge states in the bulk which can result in backscattering by enhancing the inter-edge interaction. However, this is a finite size effect, and we can use statistics in our favor to increase the uniformity of the characteristics of individual ribbons by using wider ribbons. With increasing width of the TI ribbon the variance in the transmission of different samples decreases, as shown in the supplementary figure 1.

Finally, materials with greater spin–orbit coupling, i.e. a larger gap, feature a stronger localisation of the edge states towards edges, which may alleviate this issue. To get an idea how a different materials choice will affect our results, we investigate a 2D TI ribbon with a larger bulk bandgap in the next section.

3.5. The impact of the spin–orbit coupling strength

To investigate the effect of a 2D TI with stronger spin–orbit coupling strength, or, equivalently a larger bandgap, we calculate the transmission and the local spectral charge current for a TI ribbon with a higher spin–orbit coupling strength ($\Lambda_{so} = 15$ meV). The bulk bandgap for the ribbon with increased spin–orbit coupling $\Lambda_{so} = 15$ meV is $E_g = 0.16$ eV, which is close to the theoretically predicted bulk band-gap

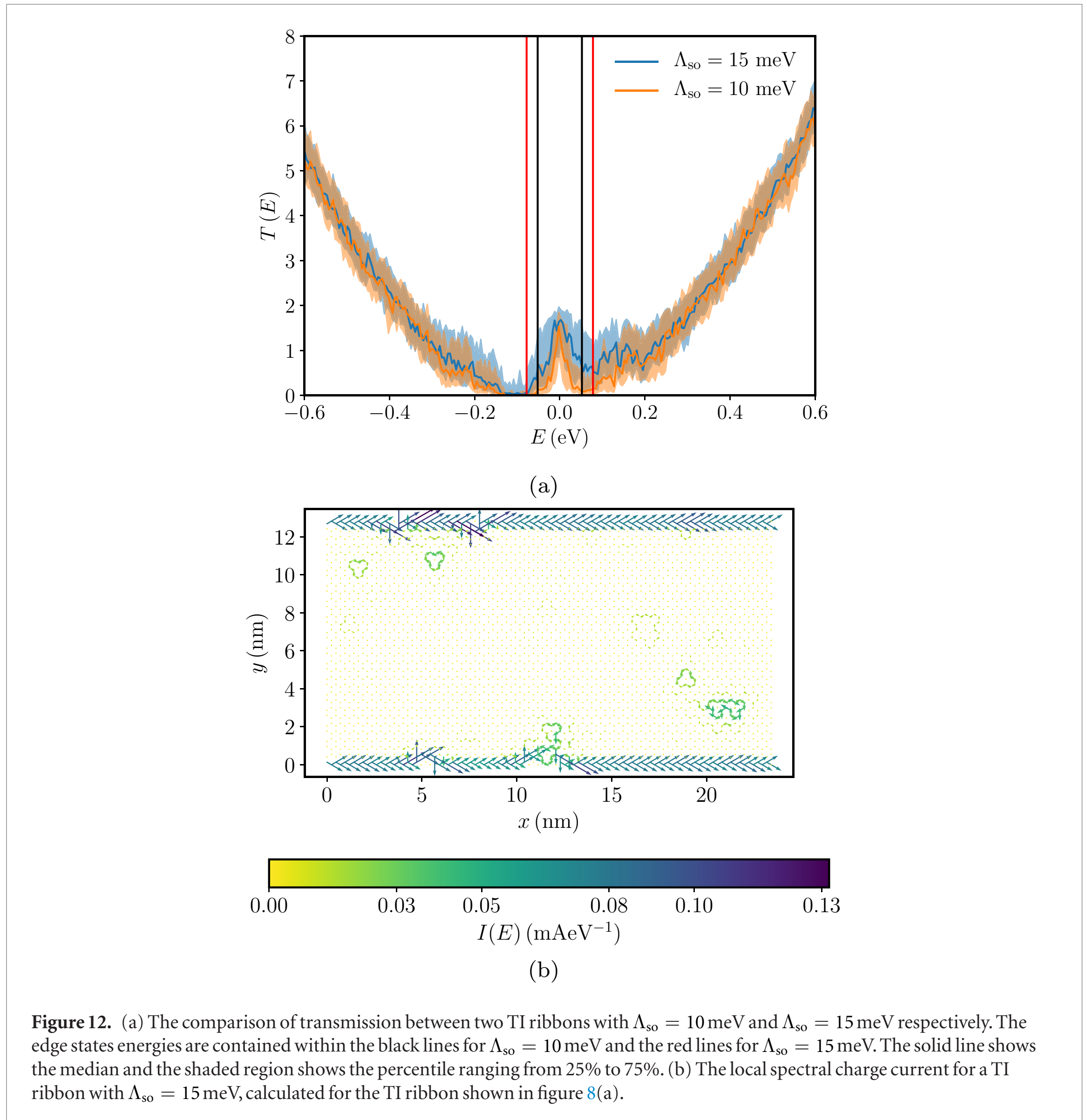

Figure 12. (a) The comparison of transmission between two TI ribbons with $\Lambda_{so} = 10$ meV and $\Lambda_{so} = 15$ meV respectively. The edge states energies are contained within the black lines for $\Lambda_{so} = 10$ meV and the red lines for $\Lambda_{so} = 15$ meV. The solid line shows the median and the shaded region shows the percentile ranging from 25% to 75%. (b) The local spectral charge current for a TI ribbon with $\Lambda_{so} = 15$ meV, calculated for the TI ribbon shown in figure 8(a).

of the stanene grown on an InSb substrate [38] and functionalized with I (iodine).

Figure 12(a) shows the comparison of transmission between the TI ribbons with spin–orbit coupling strength $\Lambda_{so} = 10$ meV and $\Lambda_{so} = 15$ meV for a random defect density of 3%. As before, we simulate 50 different defect configurations for both cases, again plotting the median and the 25th and 75th percentile. We see that the ribbons with a higher spin–orbit coupling, in general, show a higher edge state transmission over a wider energy range, while the bulk state transmission is very similar for both cases. Bulk state transmission depends on the width confinement of the ribbon and hence remains almost the same for TI ribbons of the same width but with different band gap.

Figure 12(b), further shows that the local spectral charge current penetrates less into the bulk compared to the ribbon with a lower spin–orbit coupling, as shown in figure 9(b). The higher spin–orbit coupling in 2D TI materials with a larger bandgap results in more edge state localisation in their ribbons, leading to reduced inter-edge interactions. This results in better protection against backscattering by defects, which in turn explains the increased transmission observed for the edge states in figure 12(a).

The TI-FET operation relies on an initial drop in transmission in a limited number of bulk modes near the bulk band gap. A very large spin–orbit coupling may instead lead to a scenario where more modes are available in the bulk. In such a situation, we may not be able to attain a transmission graph as shown in figure 12(a), which gives us a region with a small number of bulk modes that are strongly suppressed. Therefore, in the selection of an optimal 2D TI channel material for a TI-FET with optimal T_{ON}/T_{OFF} and low variability, there is a trade-off between the band gap (spin–orbit coupling) of the 2D TI itself and the width and defect density restrictions of the ribbon.

4. Conclusions

We have investigated electronic transport in 2D TI ribbons with a hexagonal lattice structure and zigzag edge orientation using the Kane–Mele Hamiltonian.

Our results were obtained for TI ribbons with realistic parameters, obtained by fitting our model to the DFT bandstructure of bulk stanene.

We have shown that vacancy defects in the channel modify the transmission probability significantly for conventional bulk states while the transmission of edge states is dependent on the density of defects in the ribbon. For defect concentrations up to 2%, we have shown that the 2D TI edge states are fairly robust. However, for a random defect density exceeding 4%, we have shown a significantly decreased edge state transmission. The reduced edge state transmission has been explained by an increased inter-edge interaction mediated by localised edge states around the defect centres in the bulk of the ribbon. At large defect density concentrations, the relative proximity of these localised states creates a path from one edge to the other, facilitating backscattering.

We have shown that the inclusion of vacancy defects shows a sharp decrease in the bulk state transmission near the edge of the bulk conduction and valence bands. The sharp drop in the transmission, when sweeping from the edge states near the Dirac cone to the bulk states of either band, can be exploited in the realization of TI-FETs, which operate on the principle of modulating scattering through external gating. We have estimated that only considering the coherent scattering on vacancies of a high defect distribution of 2% can produce an I_{ON}/I_{OFF} ratio of up to two orders of magnitude. Sufficiently wide ribbons should be used to reduce the variability in the transmission coefficients, and thus device characteristics of the TI-FET.

We have further demonstrated that the robustness of the TI edge states depends on the spin–orbit coupling, with a stronger spin–orbit coupling (such as in functionalized stanene) leading to less inter-edge interaction and bulk localisation for the edge states. This leads to a more robust edge state transmission and better device characteristics with reduced variability. However, we found that the transmission of the 'bulk states', for energies outside the bulk bandgap, is not necessarily reduced for a 2D TI with very high spin–orbit coupling. Because of this trade-off, we conclude that a co-optimization of the defect density and the selection of the 2D TI material (which determines the band gap) is crucial in the realization of performant TI-FETs. While defects in TI ribbons show promise for the realization of TI-FETs, reaching practical I_{ON}/I_{OFF} ratios of three orders of magnitude may require an additional (incoherent) scattering mechanisms to reduce the transmission of the bulk states even further.

Finally, we would like to mention that our calculations were performed using a Hamiltonian valid for general 2D TIs with hexagonal lattice structure (which we parameterised using the parameters of bulk stanene), experimental confirmation could be realized in existing low-bandgap 2D TIs at low temperature, or emerging high-bandgap 2D TIs at room temperature. Progressive ion bombardment of the 2D TI can introduce an increasing defect concentration in the material and could be used as a method to demonstrate the effect mentioned in this paper, experimentally.

Acknowledgments

This material is based in part upon work supported by the National Science Foundation under Grant Number 1710066.

The project or effort depicted was or is sponsored by the Department of Defense, Defense Threat Reduction Agency. The content of the information does not necessarily reflect the position or the policy of the federal government, and no official endorsement should be inferred.

This work was supported by imec's Industrial Affiliation Program.

ORCID iDs

Sabyasachi Tiwari https://orcid.org/0000-0002-2216-3893

Maarten L Van de Put https://orcid.org/0000-0001-9179-6443

Bart Sorée, https://orcid.org/0000-0002-4157-1956

William G Vandenberghe https://orcid.org/0000-0002-6717-5046

References

[1] Fischetti M V, Fu B and Vandenberghe W G 2013 Theoretical study of the gate leakage current in sub-10 nm field-effect transistors *IEEE Trans. Electron Devices* **60** 3862–9

[2] Prunnila M, Ahopelto J and Gamiz F 2004 Electron mobility in ultrathin silicon-on-insulator layers at 4.2 k *Appl. Phys. Lett.* **84** 2298–300

[3] 2016 Expanding our 2d vision *Nat. Rev. Mater.* **1** 16089

[4] Das S, Robinson J A, Dubey M, Terrones H and Terrones M 2015 Beyond graphene: progress in novel two-dimensional materials and van der waals solids *Ann. Rev. Mater. Res.* **45** 1–27

[5] Novoselov K S, Geim A K, Morozov S V, Jiang D, Zhang Y, Dubonos S V, Grigorieva I V and Firsov A A 2004 Electric field effect in atomically thin carbon films *Science* **306** 666–9

[6] Houssa M, Scalise E, Sankaran K, Pourtois G, Afanas'ev V V and Stesmans A 2011 Electronic properties of hydrogenated silicene and germanene *Appl. Phys. Lett.* **98** 223107

[7] Zólyomi V, Wallbank J R and Fal'ko V I 2014 Silicane and germanane: tight-binding and first-principles studies *2D Mater.* **1** 011005

[8] Wang Q H, Kalantar-Zadeh K, Kis A, Coleman J N and Strano M S 2012 Electronics and optoelectronics of two-dimensional transition metal dichalcogenides *Nat. Nanotechnol.* **7** 699

[9] Gaddemane G, Vandenberghe W G, Van de Put M L, Chen S, Tiwari S, Chen E and Fischetti M V 2018 Theoretical studies of electronic transport in monolayer and bilayer phosphorene: a critical overview *Phys. Rev.* B **98** 115416

[10] Podzorov V, Gershenson M E, Kloc C, Zeis R and Bucher E 2004 High-mobility field-effect transistors based on transition metal dichalcogenides *Appl. Phys. Lett.* **84** 3301–3

[11] Radisavljevic B, Radenovic A, Brivio J, Giacometti V and Kis A 2011 Single-layer mos2 transistors *Nat. Nanotechnol.* **6** 147

[12] Sarkar D, Xie X, Liu W, Cao W, Kang J, Gong Y, Kraemer S, Ajayan P M and Banerjee K 2015 A subthermionic tunnel field-effect transistor with an atomically thin channel *Nature* **526** 91

[13] Ilatikhameneh H, Tan Y, Novakovic B, Klimeck G, Rahman R and Appenzeller J 2015 Tunnel field-effect transistors in 2D transition metal dichalcogenide materials *IEEE J. Explor. Solid-State Comput. Devices Circuits* **1** 12–8

[14] McDonnell S, Addou R, Buie C, Wallace R M and Hinkle C L 2014 Defect-dominated doping and contact resistance in mos2 *ACS Nano* **8** 2880–8

[15] Lin Z, Carvalho B R, Kahn E, Lv R, Rao R, Terrones H, Pimenta M A and Terrones M 2016 Defect engineering of two-dimensional transition metal dichalcogenides *2D Mater.* **3** 022002

[16] Vandenberghe W G and Fischetti M V 2017 Imperfect two-dimensional topological insulator field-effect transistors *Nat. Commun.* **8** 14184

[17] Kane C L and Mele E J 2005 Z_2 topological order and the quantum spin hall effect *Phys. Rev. Lett.* **95** 146802

[18] Moore J E 2010 The birth of topological insulators *Nature* **464** 194

[19] Hasan M Z and Kane C L 2010 Colloquium: topological insulators *Rev. Mod. Phys.* **82** 3045–67

[20] Yokoyama T and Murakami S 2014 Spintronics and spincaloritronics in topological insulators *Physica* E **55** 1–8

[21] Yao L-Z, Crisostomo C P, Yeh C-C, Lai S-M, Huang Z-Q, Hsu C-H, Chuang F-C, Lin H and Bansil A 2015 Predicted growth of two-dimensional topological insulator thin films of III–V compounds on si(1 1 1) substrate *Sci. Rep.* **5** 15463

[22] Chen Y, Zhao C, Chen S, Du J, Tang P, Jiang G, Zhang H, Wen S and Tang D 2014 Large energy, wavelength widely tunable, topological insulator Q-switched erbium-doped fiber laser *IEEE J. Sel. Top. Quantum Electron.* **20** 315–22

[23] Chen Y, Wu M, Tang P, Chen S, Du J, Jiang G, Li Y, Zhao C, Zhang H and Wen S 2014 The formation of various multi-soliton patterns and noise-like pulse in a fiber laser passively mode-locked by a topological insulator based saturable absorber *Laser Phys. Lett.* **11** 055101

[24] Xu Y, Yan B, Zhang H-J, Wang J, Xu G, Tang P, Duan W and Zhang S-C 2013 Large-gap quantum spin hall insulators in tin films *Phys. Rev. Lett.* **111** 136804

[25] Fang Y, Huang Z-Q, Hsu C-H, Li X, Xu Y, Zhou Y, Wu S, Chuang F-C and Zhu Z-Z 2015 Quantum spin hall states in stanene/ge(1 1 1) *Sci. Rep.* **5** 14196

[26] Kresse G and Furthmüller J 1996 Efficient iterative schemes for *ab initio* total-energy calculations using a plane-wave basis set *Phys. Rev.* B **54** 11169–86

[27] Blöchl P E 1994 Projector augmented-wave method *Phys. Rev.* B **50** 17953–79

[28] Perdew J P, Burke K and Ernzerhof M 1996 Generalized gradient approximation made simple *Phys. Rev. Lett.* **77** 3865–8

[29] Fishchetti W G and Vandenberghe M V 2018 *Advanced Physics of Electron Transport in Semionductors and Nanostructures* (Berlin: Springer) (https://doi.org/10.1007/978-3-319-01101-1)

[30] Lake R, Klimeck G, Bowen R C and Jovanovic D 1997 Single and multiband modeling of quantum electron transport through layered semiconductor devices *J. Appl. Phys.* **81** 7845–69

[31] Lent C S and Kirkner D J 1990 The quantum transmitting boundary method *J. Appl. Phys.* **67** 6353–9

[32] Feynman R P 1939 Forces in molecules *Phys. Rev.* **56** 340–3

[33] Van Dyke J S and Morr D K 2017 Effects of defects and dephasing on charge and spin currents in two-dimensional topological insulators *Phys. Rev.* B **95** 045151

[34] Anderson P W 1958 Absence of diffusion in certain random lattices *Phys. Rev.* **109** 1492–505

[35] Sablikov V A and Sukhanov A A 2015 Electronic states induced by nonmagnetic defects in two-dimensional topological insulators *Phys. Rev.* B **91** 075412

[36] Lu J, Shan W-Y, Lu H-Z and Shen S-Q 2011 Non-magnetic impurities and in-gap bound states in topological insulators *New J. Phys.* **13** 103016

[37] Shan W-Y, Lu J, Lu H-Z and Shen S-Q 2011 Vacancy-induced bound states in topological insulators *Phys. Rev.* B **84** 035307

[38] Suarez Negreira A, Vandenberghe W G and Fischetti M V 2015 *Ab initio* study of the electronic properties and thermodynamic stability of supported and functionalized two-dimensional sn films *Phys. Rev.* B **91** 245103